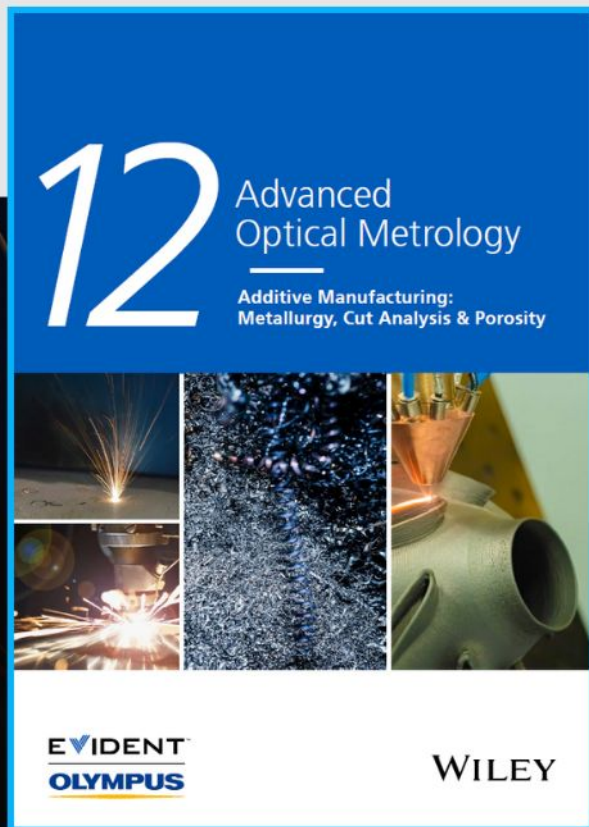




Additive Manufacturing: Metallurgy, Cut Analysis & Porosity

The latest eBook from
Advanced Optical Metrology.
Download for free.



In industry, sector after sector is moving away from conventional production methods to additive manufacturing, a technology that has been recommended for substantial research investment.

Download the latest eBook to read about the applications, trends, opportunities, and challenges around this process, and how it has been adapted to different industrial sectors.

EVIDENT™
OLYMPUS

WILEY

X-Ray Photon Correlation Spectroscopy Towards Measuring Nanoparticle Diameters in Biological Environments Allowing for the In Situ Analysis of their Bio-Nano Interface

Ferdinand Otto, Xing Sun, Florian Schulz, Carlos Sanchez-Cano, Neus Feliu, Fabian Westermeier, and Wolfgang J. Parak*

X-ray photon correlation spectroscopy (XPCS), a synchrotron source-based technique to measure sample dynamics, is used to determine hydrodynamic diameters of gold nanoparticles (Au NPs) of different sizes in biological environments. In situ determined hydrodynamic diameters are benchmarked with values obtained by dynamic light scattering. The technique is then applied to analyze the behavior of the Au NPs in a biological environment. First, a concentration-dependent agglomeration in the presence of NaCl is determined. Second, concentration-dependent increase in hydrodynamic diameter of the Au NPs upon the presence of proteins is determined. As X-rays in the used energy range are barely scattered by biological matter, dynamics of the Au NPs can be also detected in situ in complex biological environments, such as blood. These measurements demonstrate the possibility of XPCS for in situ analytics of nanoparticles (NPs) in biological environments where similar detection techniques based on visible light would severely suffer from scattering, absorption, and reflection effects.

1. Introduction

Colloidal NPs are recognized for their many potential applications in medicine, for example, for improved diagnosis, drug delivery, and therapy.^[1–3] An excellent established toolbox is available to characterize the properties of NPs in standardized environments (such as buffer solutions), but the characterization of the NPs in complex biological environments still remains challenging. So far, only a few techniques exist which allow for in situ characterization of NPs in tissue and in vivo.^[4] In practice, NPs can be extracted from tissue and then characterized ex vivo,^[5,6] but such characterization may not be representative of the situation in situ. Upon in vivo application, NPs undergo various interactions with the complex and often crowded environ-


ment, which may result in altered functionality, degradation, or agglomeration.^[7] Consequently, the desired biological function can be significantly inhibited. Characterization techniques to study such interactions in situ are therefore highly desirable. However, because the tissue is not transparent to visible light, many classical characterization techniques which work very well in buffer solutions cannot be applied for NPs embedded in tissue.^[8]

An important parameter of NPs in this context is their effective hydrodynamic diameter. Measurements of hydrodynamic diameters allow for monitoring of NP agglomeration^[9] (as manifested by a massive size increase), NP degradation/decomposition (as observed as size reduction), or protein adsorption (as detected by a small increase in size).^[10] Thus, monitoring the hydrodynamic diameter is a possibility for in situ characterization of the colloidal properties of NPs. An established technique to obtain effective hydrodynamic diameters from the diffusion coefficients of NPs via the Stokes–Einstein equation is dynamic light scattering (DLS). However, because nanoparticles are often in the size range of proteins, light-scattering from unbound proteins complicates the quantification of protein adsorption by DLS measurements of hydrodynamic diameters. To circumvent this, NPs with a fluorescent label can be used to measure fluctuations in fluorescence intensity instead of scattering fluctuations, and accordingly the technique is termed fluorescence correlation spectroscopy (FCS). As fluorescence just originates

F. Otto, X. Sun, F. Schulz, N. Feliu, W. J. Parak
Center for Hybrid Nanostructures (CHyN)
Universität Hamburg
Luruper Chaussee 149, 22761 Hamburg, Germany
E-mail: wolfgang.parak@uni-hamburg.de

X. Sun
Hunan University
Lushan Road (S) 2, Changsha 410012, P. R. China
C. Sanchez-Cano
Donostia International Physics Center
Paseo Manuel de Lardizabal 4, Donostia-San Sebastian 20018, Spain
C. Sanchez-Cano
Ikerbasque
Basque Foundation for Science
Plaza Euskadi 5, Bilbao 48009, Spain

N. Feliu
Fraunhofer Center for Applied Nanotechnology (IAP-CAN)
Grindelallee 117, 20146 Hamburg, Germany
F. Westermeier
Deutsches Elektronen-Synchrotron DESY
Notkestraße 85, 22607 Hamburg, Germany

 The ORCID identification number(s) for the author(s) of this article can be found under <https://doi.org/10.1002/sml.202201324>.

© 2022 The Authors. Small published by Wiley-VCH GmbH. This is an open access article under the terms of the Creative Commons Attribution-NonCommercial-NoDerivs License, which permits use and distribution in any medium, provided the original work is properly cited, the use is non-commercial and no modifications or adaptations are made.

DOI: 10.1002/sml.202201324

from the NPs, there is no interference in the signal due to free, unbound proteins. However, both DLS and FCS are optical techniques based on visible light, and due to strong background scattering, these techniques are not optimal for probing NP samples inside tissue. Diffusion coefficients can also be determined non-optically, for example by nuclear magnetic resonance spectroscopy (NMR).^[11,12] With this technique it was possible to determine hydrodynamic diameters of NPs in blood.^[13] As magnetic fields are barely absorbed by tissue,^[14] this technique is potentially suited for determining hydrodynamic diameters of NPs inside tissue. In order to achieve this, however, signal intensity-related issues need to be solved.^[13] In the context of magnetic NPs, another technique to study in situ dynamics in complex biological environments is based on dynamic magnetic susceptibility (DMS) measurements.^[15,16] By applying external magnetic fields, DMS measurements enable access to the rotational diffusive properties of the tracers. Hence, studying the stability and mobility of magnetic NPs in blood and tissue was demonstrated with this methodology.^[17]

In the present work, we introduce XPCS as an alternative approach, which is similar to DLS, though not based on the scattering of visible light, but on the scattering of X-rays by NPs. The dynamics on distinctive length-scales can be measured by exposing a system of scatterers (which here are the NPs) to coherent X-rays, resulting in an interference pattern, which reflects the spatial arrangement of the scatterers. If the spatial arrangement of these scatterers changes, for example, in the case of colloidal NPs by Brownian motion, this so-called speckle pattern alters correspondingly to these dynamics.^[18,19] By calculating the intensity autocorrelation function and by using a diffusion model the diffusion coefficient of the scatterers, that is, the NPs, and thus their hydrodynamic diameter can be determined. In fact, XPCS has become a reliable technique to study dynamics over a wide range of time- and length-scales primarily focused on dynamics on length scales in the sub-micron range and in viscous systems such as nanogels,^[20] glasses,^[21] and polymers.^[22] With regard to accurate quantification of hydrodynamic radii of colloidal particles in aqueous media, the majority of XPCS studies have been performed on NPs with diameters above 100 nm.^[23–25] Pioneering XPCS measurements of polymer-coated NPs in synovial fluids have been already reported.^[16] In the present study, XPCS is applied to observe the dynamics of small NPs in biological environments, with the goal of further expanding this technique towards medical-relevant nano-based systems.

With XPCS, the scatterers (in the present case NPs dispersed in aqueous media) are irradiated with coherent X-rays. The measured scattering intensity $I(q)$ is detected as a function of q , the momentum transfer of the elastically scattered photons, which is given by

$$q = \frac{4\pi}{\lambda} \sin\left(\frac{2\theta}{2}\right) \quad (1)$$

where λ is the wavelength of the X-ray photons and 2θ is the scattering angle.^[26] In case of an ergodic system, the dynamics of the scatterers can be quantified by calculating the normalized second-order intensity autocorrelation function $g_2(q, \tau)$ as a function of the momentum transfer q and the lag time τ given by

$$g_2(q, \tau) = \frac{\langle I(q, t) \cdot I(q, t + \tau) \rangle}{\langle I(q, t) \rangle^2} = 1 + \beta(q) |f(q, \tau)|^2 \quad (2)$$

where $\langle \dots \rangle$ denotes the temporal average over all times t and τ the lag time. The second-order autocorrelation function $g_2(q, \tau)$ can be connected to the first-order correlation function, which is referred to as the intermediate scattering function $f(q, \tau)$,^[27] by the Siegert relation as displayed in the right-hand part of Equation (2). Therein, $\beta(q)$ is the speckle contrast, that depends on the coherence properties of the X-ray beam and setup parameters. This demonstrates that XPCS can only be performed with (partially) coherent X-rays and thus $\beta > 0$. The speckle contrast corresponds to the accessible maximum of the intensity autocorrelation functions for $\tau \rightarrow 0$. For Brownian NPs, the intermediate scattering function can be expressed by an exponential function

$$f(q, \tau) = \exp[-\Gamma(q)\tau] \quad (3)$$

with the relaxation rate $\Gamma(q)$. The decay of the intermediate scattering function yields the effective diffusion coefficient $D(q)$ by

$$\Gamma(q) = D(q) \cdot q^2 \quad (4)$$

In the simple case of non-interacting Brownian particles, $D(q) = D_0$ on all length scales. Thus, the time-resolved scattering correlates to the free diffusion coefficient D_0 , enabling access to the dynamic properties of the NPs. For more complex sample systems, like dense biological materials, this simplification might not hold. Here, the possibility to probe the dynamics at different q and thus length-scales offers the possibility to gain deeper knowledge about the sample system, for example, distinguishing diffusive, ballistic, or direction-dependent NP motions.

With access to the free diffusion coefficient D_0 , the hydrodynamic diameter $d_h = 2 \cdot r_h$ can be obtained by applying the Stokes–Einstein equation,^[28]

$$D_0 = \frac{k_B T}{6\pi\eta r_h} \quad (5)$$

where k_B is the Boltzmann constant, T the absolute temperature and η the viscosity of the solvent in which the NPs are dispersed. Contrary to DLS, XPCS is not limited by multiple scattering in dense systems^[29] and is not restricted by solutions of an optically opaque nature. Hence, XPCS in principle should enable monitoring of NP dynamics in complex biological environments by providing the required selectivity/sensitivity, which in this study is experimentally assessed.

2. Results and Discussion

2.1. Measuring the Hydrodynamic Diameter of Au NPs with XPCS and Comparison with Other Methods

The in situ static and dynamic properties of poly-(isobutylene-alt-maleic anhydride) (PMA) coated Au NPs^[30] were studied in different environments by small-angle X-ray scattering (SAXS)

and XPCS. The NPs were exposed to varying concentrations of NaCl, to a differing abundance of bovine serum albumin (BSA), and to complex biological media, that is, human blood. Au NPs with sizes of approximately 13 and 50 nm were prepared by a modified synthesis protocol of Bastús et al.^[31] Subsequently, the NPs were overcoated by PMA.^[30] Details are provided in Sections S1 and S2, Supporting Information. The physicochemical properties of the Au NPs were characterized by UV-vis absorption spectroscopy, DLS, and zeta-potential measurements (see Section S3, Supporting Information).^[30] The core diameter d_c of the NPs was determined by transmission electron microscopy (TEM). For the smaller species, evaluation of at least 200 NPs resulted in a core diameter of $d_{c(\text{TEM})} = 13.5 \pm 0.9$ nm. The static behavior of the colloids was investigated by measuring the scattering intensity $I(q)$ in SAXS geometry. In order to determine the core size of the NPs, scattering patterns were fitted with a model for polydisperse spheres by Aragón and Pecora.^[32] The single-particle form factor $P(q)$ applied to the SAXS data yields a core diameter of $d_{c(\text{SAXS})} = 12.5$ nm (Figure 1a), which is in good agreement with the TEM results.

The upturn of the intensity $I(q)$ at low q indicates slight agglomeration of the Au NPs in aqueous media. When using X-ray techniques at high-intensity synchrotron sources, it is important to consider potential radiation damage, especially when applied to organic/soft biological matter,^[8] such as here the polymeric surface coating of the NPs, which provides colloidal stability. The high energy density of a focused X-ray beam might affect and alter the surface chemistry of the colloidal NPs. Radiation damage was probed by investigating the scattering profiles at different photon fluxes.

To further quantify changes, the Guinier approximation was applied, which allows for assessing the radius of gyration via the intensity at low q , without assuming any particular model for the scatterers. In the case of agglomeration, the intensity signal in the so-called Guinier region (i.e., the low q region with $q \cdot r_G < 1.3$ in the case of globular aggregates^[33]) is dominated by the scattering of larger structures, inhibiting the accurate quantification of r_G and limiting its validity to certain averages. For instance, in Figure 1b it can be observed that the r_G values (in the present case r_G is displayed as $d_c/2$) are consider-

ably higher than one would expect for Au NPs with a diameter of $d_{c(\text{SAXS})} = 12.5$ nm, due to the contribution of agglomerates that is also appreciable by the upturn of intensity in Figure 1a. Because the radius of gyration determined by the Guinier approximation depends sensitively on the presence of agglomerates, it has been chosen as a parameter to probe changes in the low q region. In order to test for beam-induced agglomeration, scattering experiments were carried out at varying photon flux by adding different sets of silicon absorbers to the setup. Figure 1b shows the fitted radius of gyration as converted into NP diameter $d_{c(\text{SAXS})} = 2 \cdot r_G$ as a function of radiation dose per second. No significant changes were observed for the fitted r_G values and the scattering curves at varying beam intensities, indicating negligible beam-induced agglomeration. Scattering experiments were performed at high NP concentrations to enable sufficient signal intensity for the following time-dependent fluctuation studies and to grant high contrast in non-monomodal biological environments. The absence of beam-induced changes in the low q scattering and the high initial NP concentrations are indicative of preliminary concentration-induced agglomeration. A similar concentration-dependent agglomeration behavior has been observed for the second investigated Au NP species with a diameter of 50 nm. Samples with larger Au NPs ($d_{c(\text{TEM})} = 52.5 \pm 4.8$ nm) have been measured in an ultra-small angle X-ray scattering (USAXS) setup. Form factor fitting of the scattering data resulted in a core diameter of $d_{c(\text{SAXS})} = 51.5$ nm, matching the diameter obtained by TEM (see Section S5, Supporting Information).

In situ investigation of the colloidal dynamics was carried out by recording time-dependent intensity pattern $I(q, t)$ with a coherent X-ray beam. Temporal fluctuations of the acquired interference speckle patterns give insights into the dynamics of the inorganic NPs. Figure 2a presents according to Equation (2) the intensity autocorrelation function $g_2(q, \tau)$ of 13 nm Au NPs in an aqueous medium plotted as a function of the lag time τ for $q = 0.019\text{--}0.036\text{ nm}^{-1}$. In order to highlight the very fast dynamics revealed by this plot, g_2 functions were normalized to the speckle contrast β . The rapid dynamics and limiting framing rate of the used 2D detector allow only for a partial acquisition of the autocorrelation function. Thus, fitting the relaxation rates of the $g_2(q, \tau)$ functions is restricted to a small

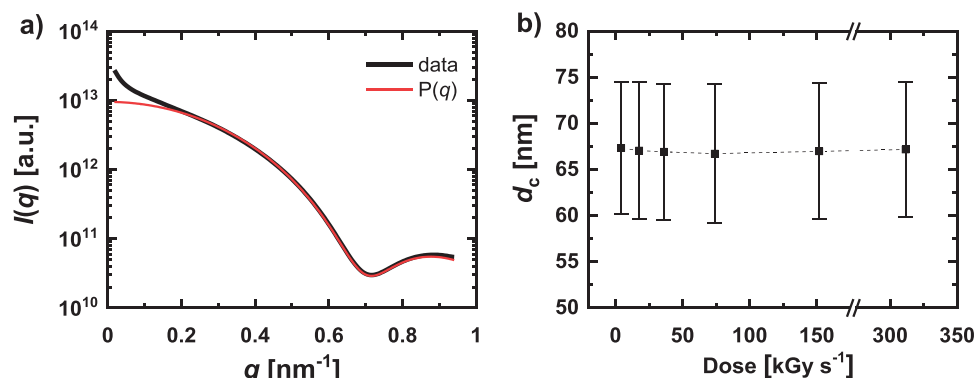


Figure 1. a) Azimuthally integrated SAXS intensity profile for 13 nm Au NPs (mass concentration $c_{\text{Au NP}} = 20\text{ mg mL}^{-1}$) were fitted with a form factor model for polydisperse spherical particles.^[32] The core radius obtained by fitting the shown SAXS data is $d_{c(\text{SAXS})} = 12.5$ nm. b) Radiation damage was excluded by investigating the scattering profiles at different photon fluxes. The fitted radius of gyration r_G is plotted as the core diameter $d_c = r_G \cdot 2$ as a function of the radiation dose per second (exact values are listed in Supporting Information).

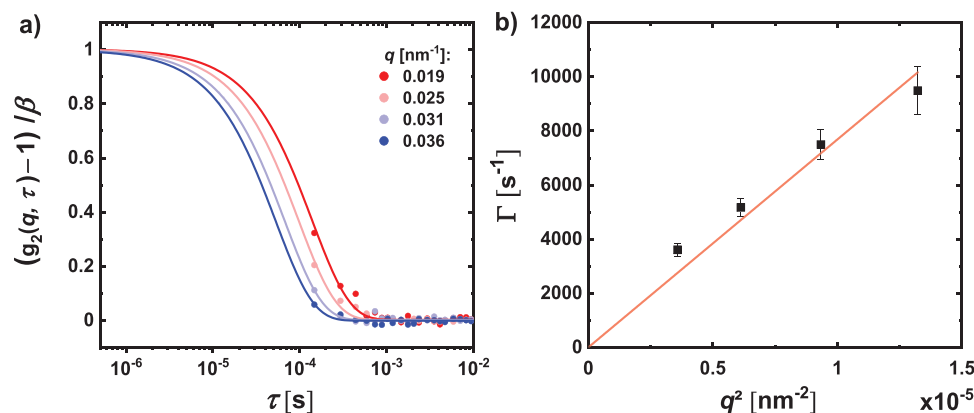


Figure 2. a) Intensity autocorrelation functions g_2 plotted as a function of the lag time τ at different q values for 13 nm Au NPs in the aqueous phase. g_2 functions were normalized to the speckle contrast ($\beta = 0.083$). Rapid dynamics of the colloids limit the accessible q range. b) Relaxation rate Γ of g_2 functions versus q^2 . The linear fit has been forced through the origin. The solid lines represent fits.

number of data points, and only the first q values are accessible, which are dominated by agglomerates. Consequently, a confident determination of the hydrodynamic diameter is not possible with this sample. Nevertheless, investigation of changes in the dynamics of the sample still provides insights into structural changes and agglomeration behavior as will be discussed in the following section regarding salt-induced agglomeration.

Despite the shortage of data points, the diffusion coefficient and the hydrodynamic diameter $d_{h(XPCS)}$ of the NPs were obtained from the autocorrelation function according to Equations (3)–(5). A free diffusion coefficient of $D_0 = 768 \cdot 10^{-12} \pm 1.28 \cdot 10^{-12} \text{ m}^2\text{s}^{-1}$ and a hydrodynamic diameter $d_{h(XPCS)} = 59.9 \pm 10.0 \text{ nm}$ were determined. As evident by the large value for d_h , precise quantification is inhibited by insufficient data points due to the rapid dynamics of such exemplary small colloids. The results were compared to the corresponding DLS values $d_{h(DLS)}$. A summary of the diameters obtained with the different methods is shown in Table 1. The organic surface coating of the NPs has been quantified previously to be on the order of a few nm.^[34] The situation $d_h \gg d_c$ here indicates the onset of some agglomeration.

2.2. Salt-Induced Agglomeration of Au NPs

As a next step, the XPCS methodology as shown in Figure 2 was applied to probe for salt-induced agglomeration of the Au NPs. Ion-mediated agglomeration is a well-known phenomenon for NPs that are stabilized by electrostatic repulsion.^[35] Here, the addition of NaCl was used to induce NP agglomeration.^[30] With increasing ionic strength, the electrostatic repulsion decreases, until the attractive van der Waals interactions

Table 1. Comparison of Au NP diameters as obtained by static ($d_{c(TEM)}$, $d_{c(SAXS)}$) and by dynamic ($d_{h(DLS)}$, $d_{h(XPCS)}$) measurements for the smaller NP specie.

| $d_{c(TEM)}$ [nm] | $d_{c(SAXS)}$ [nm] | $d_{h(DLS)}$ [nm] | $d_{h(XPCS)}$ [nm] |
|-------------------|--------------------|-------------------|--------------------|
| 13.5 ± 0.9 | 12.5 | 31.2 ± 4.2^a | 59.9 ± 10.0 |

^{a)}The DLS results show a second population peak due to NP agglomerates (see Section S3a, Supporting Information).

dominate, leading to colloidal agglomeration according to the Derjaguin–Landau–Verwey–Overbeek (DLVO) theory.^[36–39] As can be seen from the static SAXS data in Figure 3a, with increasing ionic strength the initial decay of the scattering curves at low q values becomes steeper and more pronounced, indicating the formation of agglomerates.

The XPCS data of the Au NPs exposed to the different NaCl solutions exhibit similar behavior. Figure 3b shows the respective autocorrelation functions of Au NPs at $q = 0.019 \text{ nm}^{-1}$. The slower NP diffusion dynamics due to the formation of agglomerates led to a slower decorrelation. Furthermore, at very high ion concentrations, the ongoing formation of agglomerates and thus a constant change of the scattering intensity during the individual X-ray measurements leads to a second decorrelation regime. The magnitude of this second slow decay is following the scattering intensity changes of $I(q)$ and is thus more pronounced at low q and high salt concentration. However, the typical timescale of this process is invariant of q and the salt concentration and could be interpreted as a measure of the kinetics of the agglomeration. A more detailed analysis is given in Section S8, Supporting Information.

The hydrodynamic diameters, as calculated by the fitting of the first fast relaxation process, are shown in Figure 3c as a function of the ion concentration. The determined hydrodynamic diameters are in good agreement with the static SAXS results, evidencing salt-induced agglomeration at ion concentrations above $c_{(\text{NaCl})} = 300 \text{ mM}$.

In the following, we focus our discussion on the larger Au NPs of 50 nm diameter. Due to their slower diffusion, XPCS on larger NPs is feasible with the used setup without adjusting the viscosity of the solvent, which is a common strategy to slow down dynamics.^[40] Figure 4b shows the autocorrelation function of 50 nm Au NPs ($c_{(\text{Au NP})} = 1.75 \text{ mg mL}^{-1}$) in aqueous media obtained in USAXS configuration. The slower diffusion of the larger NP species significantly improves the statistics of the dynamics. Fitting the relaxation rates $\Gamma(q)$ results in a free diffusion coefficient of $D_0 = 4.62 \cdot 10^{-12} \pm 0.23 \cdot 10^{-12} \text{ m}^2\text{s}^{-1}$. Applying the Stokes–Einstein relation, Equation (5), a hydrodynamic diameter of $d_{h(XPCS)} = 979 \pm 6.3 \text{ nm}$ is obtained. Preliminary intensity-weighted DLS measurements at lower NP concentrations indicated a hydrodynamic diameter of

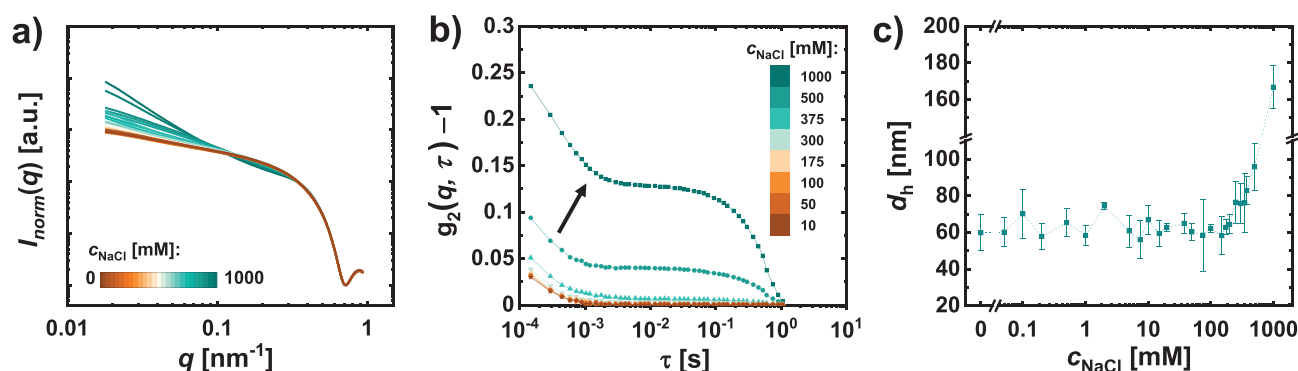


Figure 3. a) Ion-induced agglomeration behavior as determined by SAXS for 13 nm diameter Au NPs upon exposure to NaCl concentrations ranging from $c_{\text{NaCl}} = 0.05$ –1000 mM. To emphasize intensity changes at low q , the x-axis is plotted in log-scale and the scattering intensities $I(q)$ have been normalized at their minimum to $I_{\text{norm}}(q)$. b) g_2 functions at $q = 0.019 \text{ nm}^{-1}$ for different NaCl concentrations. For the sake of clarity, only a selection of concentrations is shown. c) Calculated hydrodynamic diameters d_h as a function of the corresponding NaCl concentration c_{NaCl} . The solid lines represent a guide to the eyes.

$d_{h(\text{DLS})} = 86.7 \pm 2.7 \text{ nm}$ in the absence of agglomerates. The discrepancy between the DLS and XPCS results for d_h originates from the previously discussed slight agglomeration induced by high concentrations (see Section S4, Supporting Information).

The background colors in the scattering profile in Figure 4a represent the used q range for the analysis of the dynamics, from which it is evident that the dynamics from agglomerates also contribute to the intensity autocorrelation functions. Moreover, the diffusion coefficient and hydrodynamic diameter at higher concentration ($c_{\text{Au NP}} = 3.5 \text{ mg mL}^{-1}$) were determined. A larger number of scatterers in the system increases the scattering intensity and thereby has a positive effect on the signal quality of the g_2 functions, as visible in Figure 4c. Fitting of the g_2 functions results in a larger hydrodynamic diameter of $d_{h(\text{XPCS})} = 112.5 \pm 12.6 \text{ nm}$, which agrees with the fact that higher concentrations favor NP agglomeration. The determining core and hydrodynamic diameters for the 50 nm Au NPs are listed in Table 2.

2.3. Protein-Adsorption Mediated Size Increase of NPs

Apart from abundant ions, biological media also generally contain proteins, which can adsorb to the surface of NPs forming

the so-called protein corona.^[41–43] The formation of the protein corona can be followed by an increase in the effective hydrodynamic diameter of the NPs. We would like to point out that due to the strong difference in electron density between the gold NP cores and the solvent water, the signal of the colloidal Au cores is easily detected, while both the polymer coating around the Au cores and proteins in suspension have a comparably small scattering length difference with water/buffer.^[44] Thus, XPCS should be an adequate methodology to analyze protein corona formation. However, proteins are highly radiation-sensitive. The aggregation process is primarily driven by the ionization of the solvent and the subsequent interaction of the resulting radicals with the proteins.^[45–47] Therefore, the exposure of the sample to the X-ray beam has to be optimized carefully. In order to minimize the radiation dose, the beam size was set to $100 \times 100 \mu\text{m}^2$ and a distance between sample and detector of approximately 21 m was used. Protein adsorption was induced by exposing the NPs to BSA solutions in phosphate-buffered saline (PBS) at different concentrations c_{BSA} . The incubation time before measurements was 2 h for all samples. The samples were placed in a sample chamber with temperature control to achieve consistent conditions during the measurements. In accordance with preliminary DLS measurements, a decrease in the free diffusion coefficient of 50 nm Au NPs with increasing

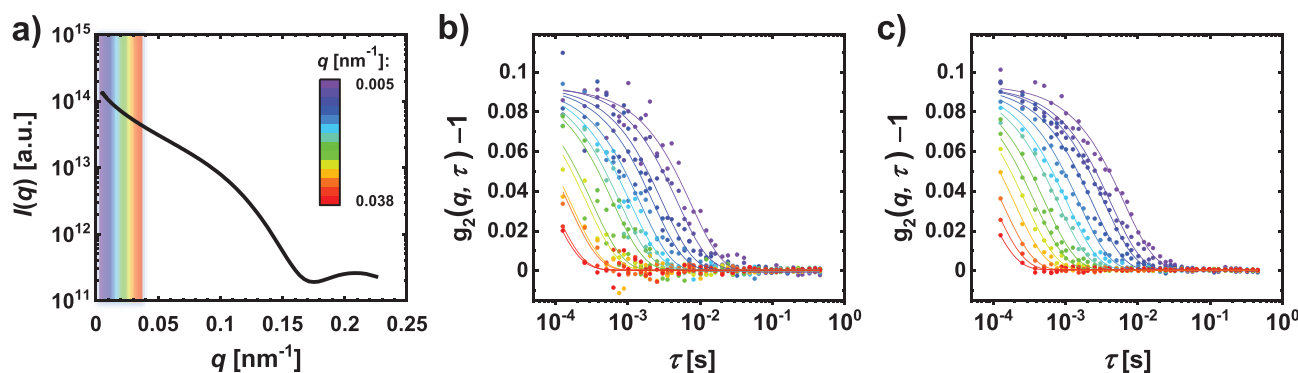


Figure 4. a) Scattering profile of 50 nm Au NPs ($c_{\text{Au NP}} = 3.5 \text{ mg mL}^{-1}$) measured in USAXS geometry. The colored background at low q corresponds to the color code for the fitted g_2 functions presented in (b,c) to emphasize the q range (0.005–0.038 nm^{-1}) used for the dynamic analysis. b) g_2 functions for 50 nm Au NPs at $c_{\text{Au NP}} = 1.75 \text{ mg mL}^{-1}$. c) g_2 functions for 50 nm Au NPs at $c_{\text{Au NP}} = 3.5 \text{ mg mL}^{-1}$. The solid lines represent fits.

Table 2. Comparison of the NP diameters as obtained by static ($d_{c(TEM)}$, $d_{c(SAXS)}$) and by dynamic ($d_{h(DLS)}$, $d_{h(XPCS)}$) measurements for the larger Au NP species.

| $d_{c(TEM)}$ [nm] | $d_{c(SAXS)}$ [nm] | $d_{h(DLS)}$ [nm] | $d_{h(XPCS)}$, 1.75 mg mL ⁻¹ [nm] | $d_{h(XPCS)}$, 3.5 mg/mL ⁻¹ [nm] |
|----------------------|-----------------------|----------------------|--|---|
| 52.5 ± 4.8 | 51.5 | 86.7 ± 2.7 | 97.9 ± 6.3 | 112.5 ± 12.6 |

BSA concentrations was observed (Figure 5a). Protein adsorption increases the hydrodynamic diameter of the NPs, thus slowing down the free diffusion. The corresponding hydrodynamic diameters are shown in Figure 5b. The alteration of dynamics with increasing protein concentrations observed by XPCS is in agreement with the intensity-weighted results of DLS measurements. Still, the dynamics obtained by XPCS show a slightly higher hydrodynamic diameter due to the presence of agglomerates as discussed before.

However, when addressing dynamics, a crucial factor to consider is the viscosity η of the investigated medium. In fact, η is a parameter in the Stokes–Einstein equation (Equation (5)). For the data shown in Figure 5b, η was assumed to be the viscosity of water at $T = 21.85^\circ\text{C}$ of $\eta_0 = 0.957\text{ mPa} \cdot \text{s}$. However, with an increased protein volume fraction, the viscosity of the solution increases, which changes the calculated hydrodynamic diameters. Precise quantification of viscosities of protein-NP solutions is rather challenging due to limiting batch volumes (due to cost reasons no large volumes are possible) or sedimentation processes during measurements (which will happen due to gravity for bigger Au NPs, even without agglomeration).^[48] We thus applied the following approximation

$$\eta = (\eta_{BSA}^* \cdot M_{w(BSA)} \cdot c_{(BSA)} + 1) \eta_0 \quad (6)$$

where η is the corrected viscosity, η_{BSA}^* is the intrinsic viscosity of the protein ($\eta_{BSA}^* = 4.13 \frac{\text{cm}^3}{\text{g}}$, Sigma-Aldrich), η_0 is the viscosity of the pure solvent (here PBS), $M_{w(BSA)}$ is the molecular weight of BSA, and $c_{(BSA)}$ denotes the protein concentration.^[49] Note that for the NaCl concentration series (Figure 3) the viscosity changed less with the used NaCl concentration, and thus the viscosity correction was neglected. In Figure 6 the

viscosity-corrected data for the BSA exposure of the NPs are shown. It is apparent that the BSA-induced increase of the hydrodynamic diameter for high BSA concentrations is no longer pronounced in the case when the concentration-corrected viscosity is used. In fact, complementary studies have shown thicknesses of a human serum albumin (HSA) protein corona around smaller NPs of around $\Delta d_h = 5\text{--}8.6\text{ nm}$.^[50–53] The size increase due to the formation of such a corona around the 50 nm NPs will be thus within the range of the experimental error.

Thus, due to the comparably large experimental error for the 50 nm NPs, the formation of the protein corona (which would add up to the NP diameter only a small fraction) could not be observed. However, the data is well suited to rule out protein-induced agglomeration, as agglomerates much larger than the size of the individual NPs are not found. For the smaller 13 nm, NPs protein adsorption results in a significantly larger percentual change, but here a faster detector would be required to resolve the diffusion dynamics. Still, with the existing methodology biologically relevant in situ measurements could be carried out. In general, salt and proteins may induce large agglomerates. Here, agglomeration was shown for NaCl (Figure 3), but not for exposure to BSA (Figure 6). The same approach can be now used to probe agglomeration in blood.

2.4. Probing the Feasibility of XPCS Measurements of NPs Dispersed in Human Blood

To test the applicability of XPCS in complex biological environments, the 13 nm Au NPs were exposed to human blood. Measurements on these blood samples were performed with an attenuated photon flux (attenuation factor $\gamma = 8.5$) in order to minimize the radiation damage. The acquired g_2 functions for a) the aqueous Au NPs, b) Au NPs exposed to blood, and c) pure blood are shown in Figure 7.

As expected, a significant deceleration of the NPs occurs as seen by the shift of the autocorrelation functions at the same q to longer lag times τ , which allows capturing a larger fraction of the exponential decay of the g_2 functions. The X-ray correlation signal of pure human blood (Figure 7c) displays

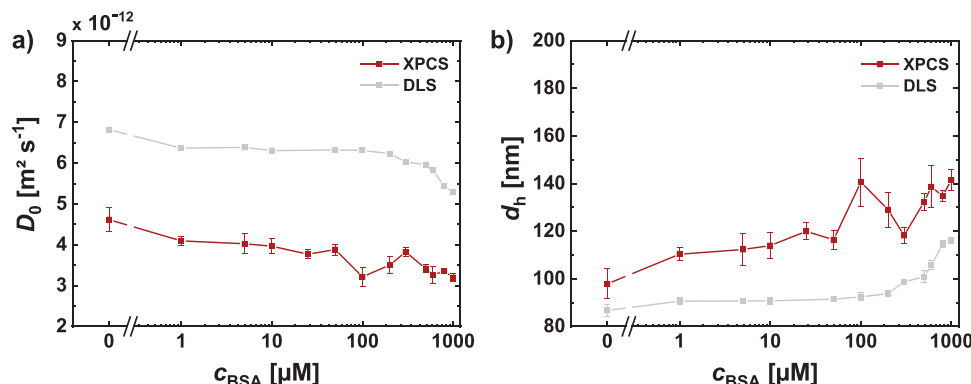


Figure 5. a) Free diffusion coefficient D_0 of PMA coated Au NPs of 50 nm core diameter as a function of the bovine serum albumin concentration $c_{(BSA)}$. Data as obtained with XPCS (red) and DLS (grey) are shown. b) Corresponding hydrodynamic diameters d_h calculated by the Stokes-Einstein law. The solid lines represent a guide to the eye.

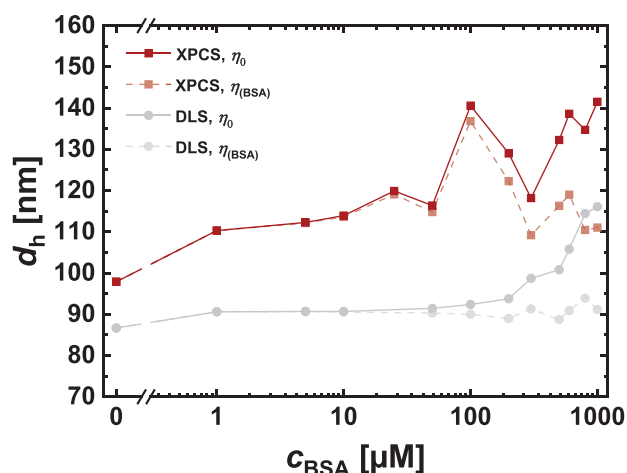


Figure 6. Hydrodynamic diameters calculated assuming a constant viscosity η_0 versus a concentration-corrected viscosity $\eta(c_{\text{BSA}})$. The solid lines are a guide to the eye.

a strong increased noise level due to the decreased scattering intensity of this control sample without NPs. At least for the smallest accessible q value ($q = 0.019 \text{ nm}^{-1}$), an exponential decay of the autocorrelation function is slightly indicated in pure blood. Relaxation of the correlation data appears at two orders of magnitude higher lag time and can thereby be associated to slow dynamics in the systems. It becomes obvious that analyzing colloidal dynamics in the blood becomes more complex as all biological components (especially larger entities like cells) contribute to a certain extent to the scattering signal. Interpretation of the data can thus be challenging, however, there are strategies to cope. For instance, scattering angle 2θ dependent analysis can assist to rule out contributions caused by direction-dependent dynamics, such as cell sedimentation, which would be relevant for NPs which have been internalized by cells. Furthermore, performing stretched exponential fits (Kohlrausch–William–Watts function) allows for a more accurate description of the dynamics in such complex systems as demonstrated in Figure 7b by the dashed lines. Another option to analyze the evolution of the probed dynamics and dynamical

heterogeneities is the calculation of the two-time correlation function, which allows access to the age-dependence of the dynamics in the investigated real-time window.^[54,55]

A direct comparison of the blood exposure to the NaCl study shows that severe agglomeration behavior during the NP exposure to blood can be excluded. However, precise quantification of the hydrodynamic diameter of the NPs in the blood remains challenging, as the non-Newtonian character of blood impedes viscosity determination. Still, for in vivo administration, it would already be helpful being able to in situ monitor the absence of larger agglomerates, which could severely clog the blood vessels.

One may also speculate about other applications of the here described technique at its current state of performance. Some studies have shown for example that the cellular distribution, targeting, and delivery of NPs to cells can be highly affected by the shear properties of biological fluid flow.^[56–59] As XPCS experiments on colloid dynamics in shear flow have been already reported,^[60] XPCS might contribute to obtaining deeper insights into the impact of shear stress on the NP distribution and their colloidal stability in complex biological fluids. Regarding the investigation of radiation-sensitive systems, X-ray studies using micro-fluidics have become a reliable strategy to mitigate radiation damage. Another promising application might be a reversed engineering approach to measure the viscosities of complex fluids by ensuring precise control over NP stability and their non-interacting nature.

The performance assessment of XPCS for the in situ analysis of NPs demonstrates the necessity of stable and well-detectable tracer NPs for future experiments. The here presented examples have shown that precise control and balancing of radiation damage, signal intensity, and sample-related experimental limitations (concentration, agglomeration, etc.) are the keys for XPCS studies of NPs in complex biological environments.

3. Conclusions and Outlook

In summary, an in situ analysis of the NP dynamics in biological environments using XPCS has been presented. Static

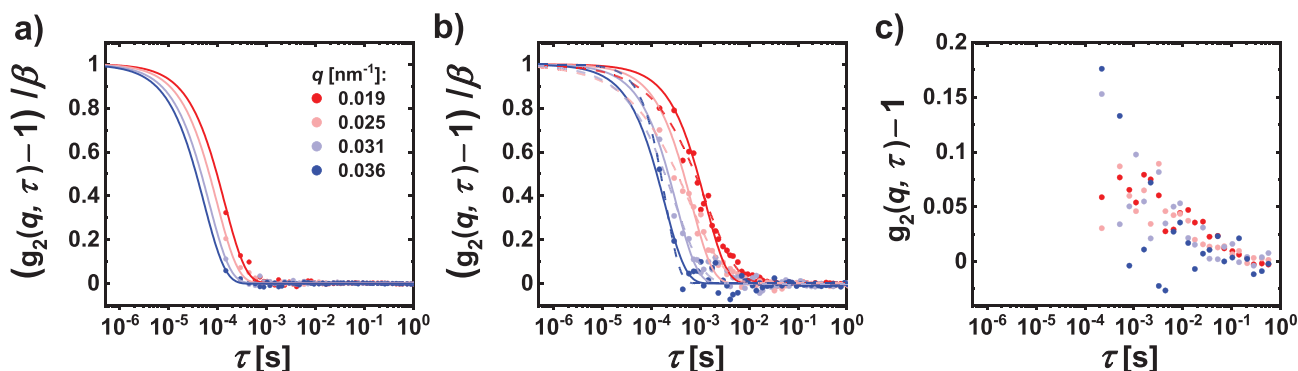


Figure 7. a) Normalized intensity autocorrelation functions of aqueous 13 nm Au NPs. Data were obtained at the highest photon flux without attenuation. b) Normalized g_2 functions of 13 nm Au NPs exposed to human blood. c) g_2 functions of pure blood as control. For the sake of clarity, the signal-to-noise ratio has been improved by repeatedly binning two consecutive data points. Non-binned data is shown in Figure S12, Supporting Information. The data shown in (b,c) were acquired at an attenuated photon flux using an attenuation factor of $\gamma = 8.5$. The solid lines represent single exponential fits and the dashed lines stretched exponential fits.

properties were obtained by analyzing the azimuthally averaged scattering intensity $I(q)$. Autocorrelation functions and hydrodynamic radii of two sub-100 nm PMA coated Au NP species in different environments were measured. Alteration of the static and dynamic properties caused by ion-induced agglomeration was investigated for the 13 nm Au NPs. The colloidal stability and protein interaction of the 50 nm Au NPs were probed by exposing them to varying BSA concentrations. Furthermore, radiation damage management and the critical role of viscosity concerning the dynamic properties were discussed. Finally, the feasibility of XPCS measurements in crowded and dynamic biological systems was demonstrated by exposing Au NPs to human blood.

It is evident that XPCS as a technique for the investigation of bio-nano interactions (e.g., agglomeration, degradation, and protein corona formation) is still in its infancy. Nevertheless, this work introduces new options and perspectives on how to circumvent present experimental limitations regarding the in situ monitoring of NPs in complex biological environments.

Probing the lower detection size limit has shown that there are definitely still restrictions due to the current detector state-of-the-art. Fortunately, with continuous development and advances in detector technology, these restrictions can be resolved in the future. Particularly noteworthy is the current transition towards fourth-generation synchrotrons all around the world. Methods like XPCS, which highly depend on the coherence property of the X-ray beam, will greatly benefit from the enhanced coherence of new generation sources.^[61,62] XPCS thus may potentially contribute considerably to novel fundamental insights on protein-NP interaction, the fate of NPs along with drug-delivery systems, and numerous other dynamics in complex biological environments. At any rate, we hope that this work highlights the potential of XPCS in the field of bionanotechnology and may serve as guidance for future XPCS experiments.

4. Experimental Section

Materials: Sodium chloride and bovine serum albumin ($\geq 96\%$) were purchased from Sigma Aldrich. HyClone phosphate-buffered saline (w/o Mg, Ca) was purchased from Cytiva. Human blood for research purposes was supplied by the Deutsches Rotes Kreuz. Quartz capillaries were obtained by Hilgenberg.

Synthesis and Characterization of Au NPs: Citrate-capped spherical gold NPs with diameters of 13 and 50 nm were synthesized in an aqueous phase using previously published protocols. For each size, the Au NP surface composition was then sequentially modified using first a ligand exchange process for transferring the NPs to organic solvent, and then overcoating with PMA for retransferring the NPs to the aqueous solution. To achieve a highly concentrated stock solution, the final NPs had been concentrated by extended centrifugation, which resulted in slight agglomeration of the NPs prior to the X-ray experiments. For the X-ray experiments, the individual samples had been diluted 1:1 from this master dispersion. The detailed experimental procedure is described in the Supporting information. The synthesized NPs were characterized by UV-vis absorption spectroscopy, DLS, TEM, and Zeta potential measurements.

Scattering Experiments: Scattering experiments were performed at the Coherence Applications Beamline P10 at PETRA III, Deutsches Elektronen-Synchrotron (DESY, in Hamburg, Germany).

Sample Preparation: The synthesized PMA-coated AuNPs were exposed to a wide range of NaCl and BSA concentrations and to the blood of two individual donors. Before the measurements, all samples were thoroughly mixed in Eppendorf tubes to ensure a homogeneous distribution. Despite the controls and the pure NP dispersions, a strict preparation protocol was followed, where the samples were incubated for 2 h at room temperature to guarantee equivalent conditions. Afterward, the samples were transferred to quartz capillaries (length of 40 mm, outer diameter of 1.0 mm and wall thickness of 0.01 mm) and were vacuum sealed. For all samples, control measurements for background subtraction without Au NPs were carried out corresponding to the investigated environment.

Coherent SAXS Setup: For SAXS experiments, X-rays were monochromatized to a photon energy of 8 keV and a photon flux of 9.1×10^{10} photons s^{-1} by a Si(111) channel cut monochromator. The beam was focused to approximately $3 \times 2 \mu m^2$ by using compound refractive lenses. The detector distance was set to 5.05 m downstream of the sample, including an evacuated flight tube between sample and detector. The direct beam was blocked by a circular beamstop in front of the detector. The scattering patterns were recorded using an Eiger X4M direct-detection hybrid pixel detector with a pixel size of $75 \times 75 \mu m^2$ and a maximum framing rate of 750 Hz, enabling access to a maximum momentum transfer q range of 0.016 to 0.94 nm^{-1} . SAXS measurements were performed with an integration time of 0.1 s over a total time period of 60 s. Speckle patterns were acquired by an EIGER X 500k Hybrid Photon Counting detector with a pixel size of $75 \times 75 \mu m^2$ and a maximum framing rate of 9 kHz. Samples were exposed for 1.4 s with a single exposure time of 0.14 ms. Measurements with the SAXS setup were performed at room temperature. In order to investigate sample alteration caused by radiation damage, measurements were carried out at varying photon fluxes by adding different sets of 25 μm thin silicon absorbers to the setup (for precise attenuation factors see Section S5, Supporting Information). With regard to photon flux variation and detector type, each sample was measured in at least 12 distinct experimental configurations.

Coherent USAXS Setup: For USAXS experiments the sample-detector distance was adjusted to 21.2 m and measurements were carried out using a photon energy of 8.54 keV and a photon flux of 2.8×10^{10} photons s^{-1} . The beam size was set to $100 \times 100 \mu m^2$. The accessible q range was 0.005 to 0.23 nm^{-1} . The samples were placed in a thermoregulated sample chamber, which has been evacuated afterward to minimize air scattering. USAXS measurements were performed at 21.85 °C. The remaining experimental procedure was analogous to the SAXS setup.

Statistical Analysis: The acquired scattering patterns were azimuthally integrated and normalized to the ring current. For static SAXS analysis, 600 frames and for dynamic XPCS measurements 10 000 frames were recorded. The data was binned in 250 (static analysis) and 18 (dynamic analysis) regions of interest and assigned to the mean q value of this bin. Static and dynamic analyses were carried out by the software package XPCSGUI written in MATLAB®.

Supporting Information

Supporting Information is available from the Wiley Online Library or from the author.

Acknowledgements

This work was supported by the Deutsche Forschungsgemeinschaft (DFG GRK 2536) and by Fraunhofer Attract (Fraunhofer-Gesellschaft). X.S. is grateful to Chinese Scholarship Council (CSC) for a PhD fellowship. The authors acknowledge DESY (Hamburg, Germany), a member of the Helmholtz Association HGF, for the provision of

experimental facilities. Parts of this research were carried out at PETRA III beamline P10. Beamtime was allocated for proposal I20180824. Open access funding enabled and organized by Projekt DEAL.

Conflict of Interest

The authors declare no conflict of interest.

Data Availability Statement

The data that support the findings of this study are available on request from the corresponding author. The data are not publicly available due to privacy or ethical restrictions.

Keywords

colloidal nanoparticles, diffusion, protein corona, small-angle X-ray scattering, X-ray photon correlation spectroscopy

Received: March 1, 2022

Revised: June 6, 2022

Published online: July 29, 2022

- [1] B. Pelaz, C. Alexiou, R. A. A. Puebla, F. Alves, A. M. Andrews, S. Ashraf, L. P. Balogh, L. Ballerini, A. Bestetti, C. Brendel, S. Bosi, M. Carril, W. C. W. Chan, C. Chen, X. Chen, X. Chen, Z. Cheng, D. Cui, J. Du, C. Dullin, A. Escudero, N. Feliu, M. Gao, M. George, Y. Gogotsi, A. Grünweller, Z. Gu, N. Halas, N. Hampp, R. K. Hartmann, et al., *ACS Nano* **2017**, *11*, 2313.
- [2] S. Bayda, M. Adeel, T. Tuccinardi, M. Cordani, F. Rizzolio, *Molecules* **2019**, *25*, 112.
- [3] R. A. Sperling, P. Rivera Gil, F. Zhang, M. Zanella, W. J. Parak, *Chem. Soc. Rev.* **2008**, *37*, 1896.
- [4] J. M. Perez, L. Josephson, T. O'Loughlin, D. Hogemann, R. Weissleder, *Nat. Biotechnol.* **2002**, *20*, 816.
- [5] M. Hadjidemetriou, Z. Al-Ahmady, K. Kostarelos, *Nanoscale* **2016**, *8*, 6948.
- [6] R. García-Álvarez, M. Hadjidemetriou, A. Sánchez-Iglesias, L. M. Liz-Marzán, K. Kostarelos, *Nanoscale* **2018**, *10*, 1256.
- [7] N. Feliu, D. Docter, M. Heine, P. Del Pino, S. Ashraf, J. Kolosnjaj-Tabi, P. Macchiarini, P. Nielsen, D. Alloyeau, F. Gazeau, R. H. Stauber, W. J. Parak, *Chem. Soc. Rev.* **2016**, *45*, 2440.
- [8] C. Sanchez-Cano, R. A. Alvarez-Puebla, J. M. Abendroth, T. Beck, R. Blick, Y. Cao, F. Caruso, I. Chakraborty, H. N. Chapman, C. Chen, B. E. Cohen, A. L. C. Conceição, D. P. Cormode, D. Cui, K. A. Dawson, G. Falkenberg, C. Fan, N. Feliu, M. Gao, E. Gargioni, C.-C. Glüer, F. Grüner, M. Hassan, Y. Hu, Y. Huang, S. Huber, N. Huse, Y. Kang, A. Khademhosseini, T. F. Keller, et al., *ACS Nano* **2021**, *15*, 3754.
- [9] N. Hondow, R. Brydson, P. Wang, M. D. Holton, M. R. Brown, P. Rees, H. D. Summers, A. Brown, *J. Nanopart. Res.* **2012**, *14*, 977.
- [10] J. Piella, N. G. Bastús, V. Puentes, *Bioconjugate Chem.* **2017**, *28*, 88.
- [11] D. Padro, P. Cienskowski, S. Lopez-Fernandez, I. Chakraborty, C. Carrillo-Carrion, N. Feliu, W. J. Parak, M. Carril, *Small* **2020**, *16*, 2001160.
- [12] C. Zhang, Z. Jin, B. Zeng, W. Wang, G. Palui, H. Mattoussi, *J. Phys. Chem. B* **2020**, *124*, 4631.
- [13] M. Carril, D. Padro, P. D. Pino, C. Carrillo-Carrion, M. Gallego, W. J. Parak, *Nat. Commun.* **2017**, *8*, 1542.
- [14] D. Formica, S. Silvestri, *Biomed. Eng. Online* **2004**, *3*, 11.
- [15] A. C. Bohorquez, C. Yang, D. Bejleri, C. Rinaldi, *J. Colloid Interface Sci.* **2017**, *506*, 393.
- [16] M. Unni, S. Savliwala, D. Partain Brittany, L. Maldonado-Camargo, Q. Zhang, S. Narayanan, M. Dufresne Eric, J. Ilavsky, P. Grybos, A. Koziol, P. Maj, R. Szczygiel, D. Allen Kyle, M. Rinaldi-Ramos Carlos, *Sci. Adv.* **2021**, *7*, abf8467.
- [17] A. C. Bohorquez, M. Unni, S. Belsare, A. Chiu-Lam, L. Rice, C. Pampo, D. Siemann, C. Rinaldi, *Bioconjugate Chem.* **2018**, *29*, 2793.
- [18] M. Sutton, S. G. J. Mochrie, T. Greytak, S. E. Nagler, L. E. Berman, G. A. Held, G. B. Stephenson, *Nature* **1991**, *352*, 608.
- [19] F. Lehmkuhler, W. Roseker, G. Grübel, *Appl. Sci.* **2021**, *11*, 6179.
- [20] A. Jain, F. Schulz, I. Lokteva, L. Frenzel, G. Grübel, F. Lehmkuhler, *Soft Matter* **2020**, *16*, 2864.
- [21] B. Ruta, G. Baldi, Y. Chushkin, B. Rufflé, L. Cristofolini, A. Fontana, M. Zanatta, F. Nazzari, *Nat. Commun.* **2014**, *5*, 3939.
- [22] H. Conrad, F. Lehmkuhler, B. Fischer, F. Westermeier, M. A. Schroer, Y. Chushkin, C. Gutt, M. Sprung, G. Grübel, *Phys. Rev. E* **2015**, *91*, 042309.
- [23] T. Autenrieth, A. Robert, J. Wagner, G. Grübel, *J. Appl. Crystallogr.* **2007**, *40*, s250.
- [24] G. Grübel, D. L. Abernathy, D. O. Riese, W. L. Vos, G. H. Wegdam, *J. Appl. Crystallogr.* **2000**, *33*, 424.
- [25] F. Westermeier, B. Fischer, W. Roseker, G. Grübel, G. ägele, M. Heinen, *J. Chem. Phys.* **2012**, *137*, 114504.
- [26] J. Als-Nielsen, D. McMorrow, *Elements of Modern X-ray Physics*, John Wiley & Sons, Inc., Hoboken, NJ **2011**.
- [27] G. Grübel, F. Zontone, *J. Alloys Compd.* **2004**, *362*, 3.
- [28] J.-P. Hansen, I. R. McDonald, *Theory of Simple Liquids*, 3rd ed., Academic Press, Cambridge, MA **2006**.
- [29] D. O. Riese, W. L. Vos, G. H. Wegdam, F. J. Poelwijk, D. L. Abernathy, G. Grubel, *Phys. Rev. E* **2000**, *61*, 1676.
- [30] J. Hühn, C. Carrillo-Carrion, M. G. Soliman, C. Pfeiffer, D. Valdeperez, A. Masood, I. Chakraborty, L. Zhu, M. Gallego, Y. Zhao, M. Carril, N. Feliu, A. Escudero, A. M. Alkilany, B. Pelaz, P. d. Pino, W. J. Parak, *Chem. Mater.* **2017**, *29*, 399.
- [31] N. G. Bastus, J. Comenge, V. Puentes, *Langmuir* **2011**, *27*, 11098.
- [32] S. R. Aragón, R. Pecora, *J. Chem. Phys.* **1975**, *64*, 2395.
- [33] D. A. Jacques, J. Trehwella, *Protein Sci.* **2010**, *19*, 642.
- [34] R. A. Sperling, F. Zhang, M. Zanella, S. Kudera, W. J. Parak, *J. Phys. Chem. C* **2007**, *111*, 31.
- [35] A. Bruinink, J. Wang, P. Wick, *Arch. Toxicol.* **2015**, *89*, 659.
- [36] E. J. W. Verwey, J. Th. G. Overbeek, *Theory of the Stability of Lyophobic Colloids: The Interaction of Sol Particles Having an Electric Double Layer*, Vol. 218, Elsevier, Amsterdam **1948**.
- [37] B. D. Johnston, W. G. Kreyling, C. Pfeiffer, M. Schäffler, H. Sarioglu, S. Ristig, S. Hirn, N. Haberl, S. Thalhammer, S. M. Hauck, M. Semmler-Behnke, M. Eppler, J. Hühn, P. d. Pino, W. J. Parak, *Adv. Funct. Mater.* **2017**, *27*, 1701956.
- [38] C. Pfeiffer, C. Rehbock, D. Hühn, C. Carrillo-Carrion, D. J. de Aberasturi, V. Merk, S. Barcikowski, W. J. Parak, *J. R. Soc., Interface* **2014**, *11*, 20130931.
- [39] L. T. T. Trinh, A.-L. Kjøniksen, K. Zhu, K. D. Knudsen, S. Volden, W. R. Glomm, B. Nyström, *Colloid Polym. Sci.* **2009**, *287*, 1391.
- [40] R. L. Leheny, *Curr. Opin. Colloid Interface Sci.* **2012**, *17*, 3.
- [41] T. Cedervall, I. Lynch, S. Lindman, T. Berggård, E. Thulin, H. Nilsson, K. A. Dawson, S. Linse, *Proc. Natl. Acad. Sci. USA* **2007**, *104*, 2050.
- [42] P. Chun Ke, S. Lin, W. J. Parak, T. P. Davis, F. Caruso, *ACS Nano* **2017**, *11*, 11773.
- [43] H. van Nguyen, B.-J. Lee, *Int. J. Nanomed.* **2017**, *12*, 3137.
- [44] L. A. Feigin, D. I. Svergun, *Structure Analysis by Small-Angle X-Ray and Neutron Scattering*, Plenum Press, New York **1987**.

- [45] C. M. Jeffries, M. A. Graewert, D. I. Svergun, C. E. Blanchet, *J. Synchrotron Radiat.* **2015**, 22, 273.
- [46] S. Kuwamoto, S. Akiyama, T. Fujisawa, *J. Synchrotron Radiat.* **2004**, 11, 462.
- [47] W. M. Garrison, *Chem. Rev.* **1987**, 87, 381.
- [48] N. Feliu, X. Sun, R. A. A. Puebla, W. J. Parak, *Langmuir* **2017**, 33, 6639.
- [49] G. U. Nienhaus, P. Maffre, K. Nienhaus, *Methods Enzymol.* **2013**, 519, 115.
- [50] C. Röcker, M. Pötzl, F. Zhang, W. J. Parak, G. U. Nienhaus, *Nat. Nanotechnol.* **2009**, 4, 577.
- [51] S. Ashraf, J. Park, M. Bichelberger, K. Kantner, R. Hartmann, P. Maffre, A. H. Said, N. Feliu, J. Lee, D. Lee, G. U. Nienhaus, S. Kim, W. J. Parak, *Nanoscale* **2016**, 10, 1318.
- [52] H. Wang, L. Shang, P. Maffre, S. Hohmann, F. Kirschhöfer, G. Brenner-Weiß, G. U. Nienhaus, *Small* **2016**, 12, 5836.
- [53] D. Hühn, K. Kantner, C. Geidel, S. Brandholt, I. De Cock, S. J. H. Soenen, P. Rivera Gil, J.-M. Montenegro, K. Braeckmans, K. Müllen, G. U. Nienhaus, M. Klapper, W. J. Parak, *ACS Nano* **2013**, 7, 3253.
- [54] A. Madsen, R. L. Leheny, H. Guo, M. Sprung, O. Czakkell, *New J. Phys.* **2010**, 12, 055001.
- [55] A. Girelli, H. Rahmann, N. Begam, A. Ragulska, M. Reiser, S. Chandran, F. Westermeier, M. Sprung, F. Zhang, C. Gutt, F. Schreiber, *Phys. Rev. Lett.* **2021**, 126, 138004.
- [56] T. Saxer, A. Zumbuehl, B. Müller, *Cardiovasc. Res.* **2013**, 99, 328.
- [57] M. N. Holme, I. A. Fedotenko, D. Abegg, J. Althaus, L. Babel, F. Favarger, R. Reiter, R. Tanasescu, P.-L. Zaffalon, A. Ziegler, B. Müller, T. Saxer, A. Zumbuehl, *Nat. Nanotechnol.* **2012**, 7, 536.
- [58] N. Korin, M. Kanapathipillai, B. D. Matthews, M. Crescente, A. Brill, T. Mammoto, K. Ghosh, S. Jurek, S. A. Bencherif, D. Bhatta, A. U. Coskun, C. L. Feldman, D. D. Wagner, D. E. Ingber, *Science* **2012**, 337, 738.
- [59] R. Urbani, F. Westermeier, B. Banusch, M. Sprung, T. Pfohl, *J. Synchrotron Radiat.* **2016**, 23, 1401.
- [60] S. Busch, T. H. Jensen, Y. Chushkin, A. Fluerasu, *Eur. Phys. J. E* **2008**, 26, 55.
- [61] J. Moller, M. Sprung, A. Madsen, C. Gutt, *IUCrj* **2019**, 6, 794.
- [62] T. Narayanan, H. Wacklin, O. Kononov, R. Lund, *Crystallogr. Rev.* **2017**, 23, 160.